中国激光

激光选区熔化Ti-1023合金微观组织及力学性能研究

杨子威[1,2]，徐俊强[1,2]，郭顺[1,2]，武文迪[1,2]，周琦[1,2*]

[1]南京理工大学材料科学与工程学院，江苏 南京 210094；

[2]工业和信息化部可控电弧智能增材制造技术重点实验室，江苏 南京 210094

摘要 采用真空电弧熔炼(VAM)和激光选区熔化(SLM)技术制备了Ti-1023合金试样，并对其组织性能进行了测试分析。结果表明：SLM快速冷却条件抑制了β→α的相变过程，形成了全β相组织，而VAM试样由α+β双相组织构成。虽然SLM样品缺少高硬度α相，但快速冷却条件带来的高密度位错阻碍了位错运动，使得其屈服强度与VAM试样相近。α/β相界面会阻碍位错滑移，从而导致塑性降低，而SLM试样全β相组织可避免α/β界面的产生，并在变形中产生了应力诱导马氏体相变，使得断裂延伸率提升至VAM试样的5倍以上。

关键词 激光技术；Ti-1023；激光选区熔化；真空电弧熔炼；微观组织；力学性能

中图分类号 TG456.7 **文献标志码** A **DOI**：10.3788/CJL230729

1 引 言

亚稳β钛合金具有高强度、高延展性、高耐腐蚀性、低密度、低弹性模量和良好的生物相容性等优点，在过去二十年中得到了快速发展，并被广泛应用于航天航空、生物医学以及石油化工等领域[1-3]。例如，Ti-13V-11Cr-3Al是第一种产业化的亚稳β钛合金，经过熔炼-变形-热处理后，其屈服强度最高可达到1240 MPa，曾被用于制造高速侦察机的机身[4]；Ti-10V-2Fe-3Al亚稳β合金开发于90年代后期，经过熔炼-变形-热处理后，其最高抗拉强度可达到1220 MPa，被用于制造飞机的起落架和机身承载部件等[4-5]。

亚稳β钛合金具有熔点高、活性高、热导率低以及变形抗力大等特点。然而，传统加工方式主要是通过真空电弧熔炼(VAM)或机械合金化等冶金方法制备亚稳β钛合金铸锭，后续还需要进行轧制/锻造和热处理才能获得块状亚稳β钛合金。块状亚稳β钛合金在机械加工时产生的热量很难通过工件释放，且在加工时局部温度上升快，易与空气中的氧、氢发生作用[6-9]。因此，面对航天航空复杂结构，传统制造手段存在工序多、周期长、成本高且良品率低等问题[10]。而激光选区熔化(SLM)技术是以激光为热源，通过逐层熔化金属粉末，制造出实体零件，可以实现复杂结构的近净成形，后续仅需通过热处理来调整其性能，大大简化了制备亚稳β钛合金复杂结构的工序。凭借超强的复杂结构成形能力、超高的材料利用率以及超快的原型制造速度，激光选区熔化技术为航空航天复杂结构钛合金零件的制造提供了良好的解决方案[11-13]。对于亚稳β钛合金的初步制造工艺，SLM的冷却速率为10^3～10^8 K/s^{-1}[14-15]，VAM的冷却速率为10～10^2 K/s^{-1}[16-18]。快速冷却引起的非平衡凝固有利于晶粒细化，SLM成形试样的晶粒尺寸远小于VAM成形试样，而晶粒尺寸对力学性能的影响较为显著。激光选区熔化的多功能性和快速冷却条件会带来特殊的组织和优异的力学性能，关于该技术制造不同合金(包括铝合金、钢和α/α+β钛合金)的可行性已得到大量研究，而关于激光选区熔化增材的亚稳β钛合金研究则较少[19-28]。

Ti-10V-2Fe-3Al(Ti-1023)合金是一种典型的亚稳β钛合金，该合金具有良好的热处理性能，相变点温度在795～805 ℃范围内[1]。故采用真空电弧熔炼Ti-1023合金模拟Ti-1023铸态组织，对比激光选区熔化与真空电弧熔炼Ti-1023合金的微观组织及力学性能的差异，系统研究快速冷却条件对Ti-1023合金组织和性能的影响规律。研究结果为亚稳β钛合金复杂构件的增材制造提供了参考。

2 实验方法

激光选区熔化制备SLM试样选用气雾化法制备的Ti-1023合金粉末。Ti-1023粉末形貌、粒径如图1所示。采用真空干燥箱对Ti-1023粉末进行烘干处理，避免制备过程中粉末受潮导致的气孔等缺陷。烘干温度和时间分别设定为120 ℃和2 h。采用激光金

收稿日期：2023-04-17；**修回日期**：2023-05-23；**录用日期**：2023-06-19；**网络首发日期**：2023-07-04

基金项目：国家自然基金(52105367)

通信作者：*cheezhou@njust.edu.cn

属铺粉3D打印机制备SLM试样，激光光斑直径为70 μm，将纯氩气通入成型箱中进行洗气，待成型箱中的氧气体积分数降至4×10^{-4}以下，在Ti-6Al-4V基板上直接沉积尺寸为20 mm×20 mm×10 mm的块体，如图2(a)所示。Ti-6Al-4V基板和Ti-1023粉末元素含量如表1所示。制备所使用的工艺参数为：激光功率250 W，扫描速度1100 mm/s，扫描间距60 μm，铺粉厚度30 μm，67°旋转扫描策略，如图2(b)所示，其中N为扫描层编号。采用阿基米德法进行测量，可以得到相对密度为99.9%的试样。

通过真空电弧熔炼对商用Ti-1023合金板材进行重熔处理以制备VAM试样，商用Ti-1023合金板材的元素含量如表1所示。采用电火花线切割设备将板材切割成小块体，并通过打磨、乙醇清洗等除去块体表面油污。将处理完成后的原材料置于真空电弧熔炼炉的水冷铜坩埚中，抽真空使气压低至5×10^{-4} Pa后充入氩气，并重复三次，以降低环境中的氧气含量，避免试样氧化。采用钨极引弧后将材料熔化，电弧熔炼时间设定为150 s，并采用电磁搅拌与重复熔炼相结合的方法，保证铸锭成分的均匀性。

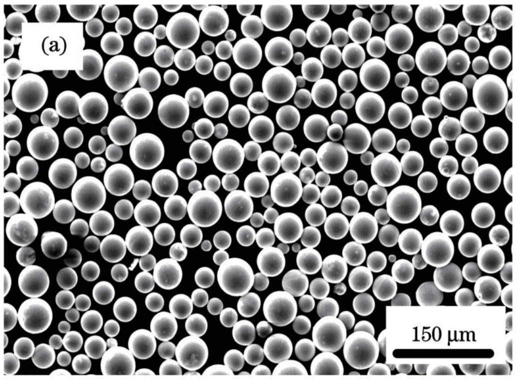

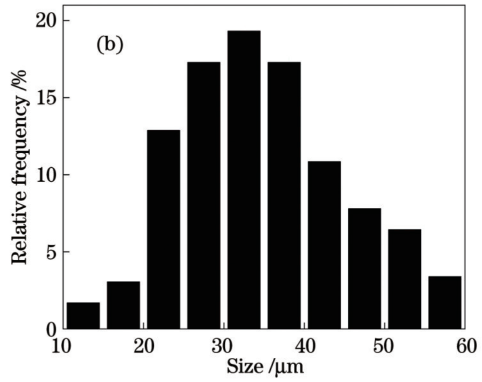

图1 Ti-1023粉末形貌及粒径分布。(a)粉末形貌；(b)粒径分布

Fig. 1 Ti-1023 powder morphology and particle size distribution. (a) Powder morphology; (b) particle size distribution

表1 Ti-1023粉末、Ti6Al4V基板和Ti-1023板材的元素含量(质量分数，%)

Table 1 Element contents of Ti-1023 powder, Ti6Al4V substrate, and Ti-1023 plate (mass fraction, %)

Element	V	Al	Fe	C	H	O	N	Ti
Ti-1023 powder	9.820	3.050	1.720	0.010	0.003	0.130	0.018	Bal.
Ti6Al4V substrate	3.800	6.200	0.300	0.100	0.015	0.200	0.050	Bal.
Ti-1023 plate	10.500	3.200	2.100	0.050	0.015	0.130	0.050	Bal.

采用电火花线切割方式获取尺寸为10 mm×10 mm×5 mm的试样进行组织观察，利用砂纸精磨试样后进行抛光处理，获得镜面试样后使用Kroll试剂腐蚀10 s。使用X射线衍射仪(XRD)对处理后的试样进行物相分析，扫描角度范围为30°~80°，步长设定为0.2，停留时间为0.3 s。采用光学显微镜(OM)、扫描电子显微镜(SEM)对试样显微组织进行观察分析。利用电子背散射衍射设备(EBSD)对不同工艺下的物相组成、位错密度等进行定量分析，测试前利用振动抛光设备处理试样表面，振动抛光频率和抛光时间分别设定为56 Hz和16 h。利用万能力学试验机对不同工艺下的Ti-1023试样的拉伸性能进行测试，测试采用板状非比例试样，不同工艺参数下拉伸3次，分别命名为VAM-1、VAM-2、VAM-3和SLM-1、SLM-2、SLM-3。板状试样的标距为8 mm，宽度为2 mm，厚度为1 mm，如图2(c)所示，拉伸速率设置为0.1 mm/min。采用XRD和SEM对拉伸后的试样的物相组成和断口进行表征分析，以探究拉伸断裂过程中的组织变化。

3 实验结果

3.1 物相组成与显微组织

图3为不同工艺条件下制备的Ti-1023合金的XRD图谱。可以看出，VAM试样的衍射峰与α相和β相的衍射峰匹配，而在SLM试样中仅发现了β相的衍射峰，说明VAM试样的物相组成为α+β相，而SLM试样主要是由β相组成的。表明在VAM过程中产生了β到α的固态相变，而在SLM过程中β到α的固态相变受到抑制。对于亚稳β钛合金而言，添加足量的β相稳定元素，如Mo、V、Fe等元素，能固溶强化基体，可在室温组织中保留足够多的亚稳β相。根据亚稳β钛合金的连续转变动力曲线可知，冷却速率对钛合金的室温组织的影响较大，当冷却速率超过822 $K\cdot s^{-1}$时室温组织均为β相，而SLM的冷却速率高达10^3~10^8 $K\cdot s^{-1}$[29]。因此，SLM Ti-1023合金的冷却速率大于亚稳β钛合金α相产生的临界冷却速率，在冷却过程中抑制β相到α相的相变，可使高温β相全部保留至室温。

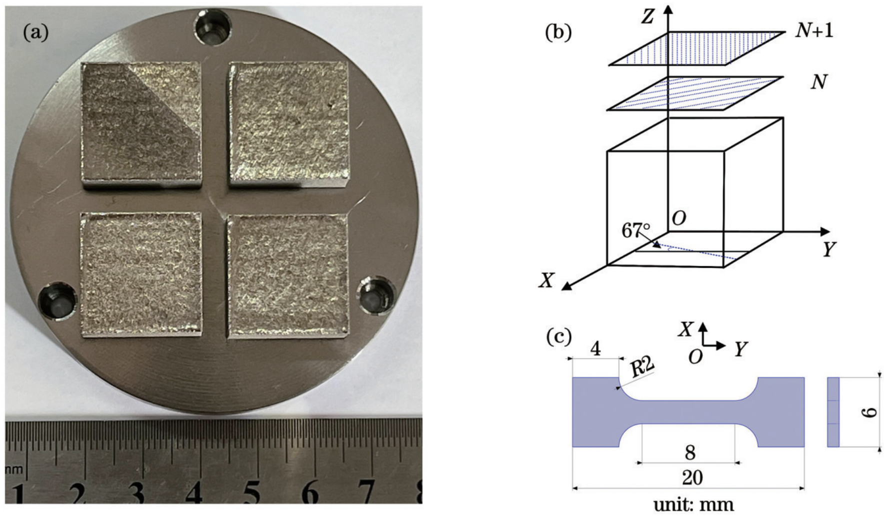

图 2　Ti-1023合金的SLM工艺流程。(a)SLM Ti-1023合金零件；(b)扫描策略示意图；(c)拉伸试样示意图

Fig. 2　SLM process flow of Ti-1023 alloy. (a) SLM Ti-1023 alloy parts; (b) schematic of scanning strategy; (c) schematic of tensile specimen

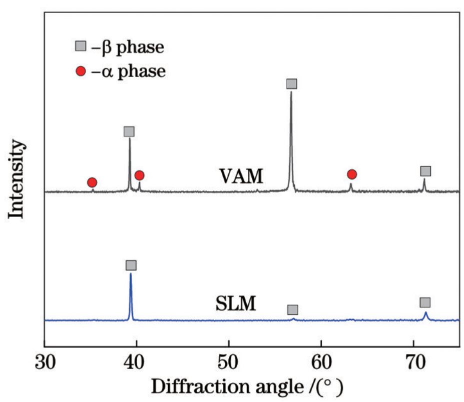

图 3　不同工艺条件下 Ti-1023合金的 XRD 谱

Fig. 3　XRD patterns of Ti-1023 alloy under different process conditions

图 4 为不同工艺条件下 Ti-1023 合金的光学显微组织及晶粒尺寸统计图。从图 4(a)、(b)可以看出，SLM 试样的熔道边界规则排列，熔道宽度约为 65 μm，层与层之间旋转 67°，平均晶粒尺寸为 47.3 μm。从图 4(c)、(d)可以看出，VAM 试样为粗大的等轴晶，平均晶粒尺寸为 510.6 μm，晶粒分布不规则，黑色衬度为 α 相，白色衬度为基体 β 相，晶粒内部的 α 相排布较为混乱，没有形成 α 相集束。说明 SLM 试样 β 晶粒尺寸约为 VAM 试样 β 晶粒尺寸的 1/10。激光选区熔化增材技术利用高能激光束熔化预铺设的金属粉末薄层，热量集中，冷却速率高。同时，熔池液态金属主要依附沉积层晶粒形核长大，熔池高温停留时间较短，晶粒来不及长大便凝固。而真空电弧熔炼技术利用钨极电弧

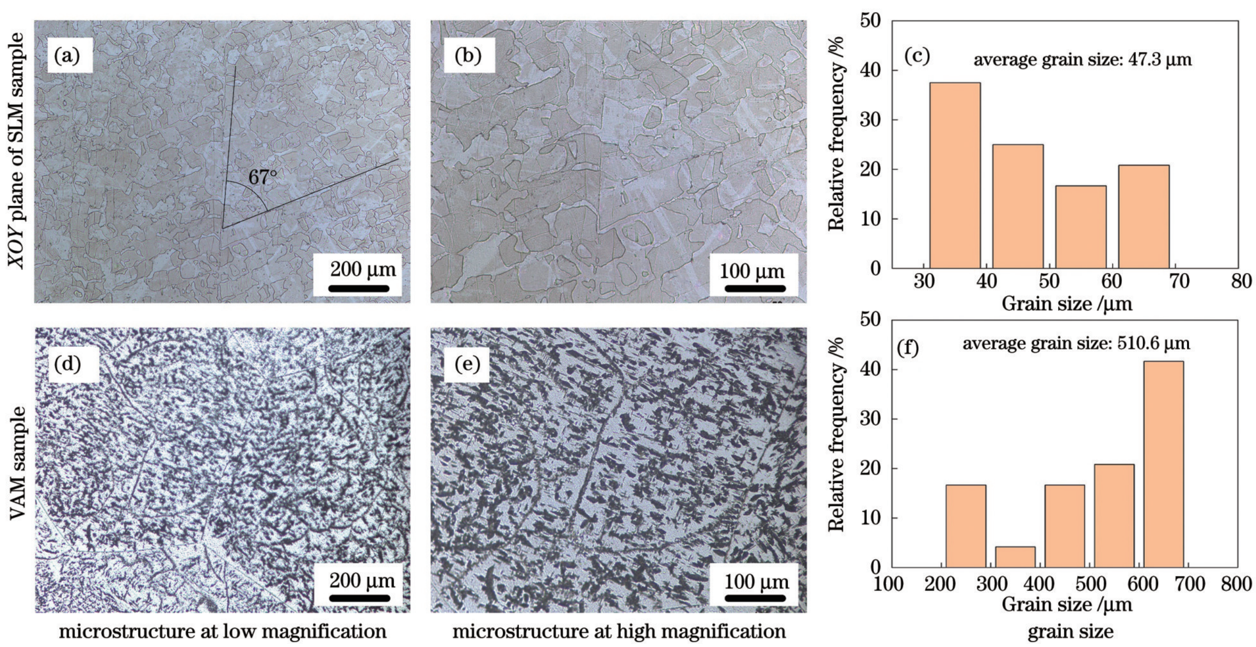

图 4　不同工艺条件下 Ti-1023合金的显微组织及晶粒尺寸统计

Fig. 4　Microstructures and grain size statistics of Ti-1023 alloy under different process conditions

熔炼金属，熔池体积远大于激光选区熔化形成的熔池，且真空电弧熔炼的冷却速率为 $10\sim10^2$ K·s^{-1}，在冷却过程中β晶粒易长大。而晶粒尺寸与力学性能紧密相关，屈服强度随着晶粒尺寸的倒数的增大而增大，即晶粒尺寸越小，强度和硬度越高。

3.2　拉伸性能

图 5 为不同工艺条件下 Ti-1023 拉伸试样的应力-应变曲线。可以看出，VAM 试样的平均屈服强度（$\sigma_{0.2}$）为 680 MPa，平均抗拉强度（σ_t）为 836 MPa，延伸率（ε_t）为 1.4%，而 SLM 试样的平均屈服强度为 600 MPa，平均抗拉强度为 1061 MPa，延伸率为 7.6%。SLM 试样与 VAM 试样的屈服强度相近，但极限抗拉强度高于 VAM 试样，且延伸率为 VAM 试样的 5 倍以上。

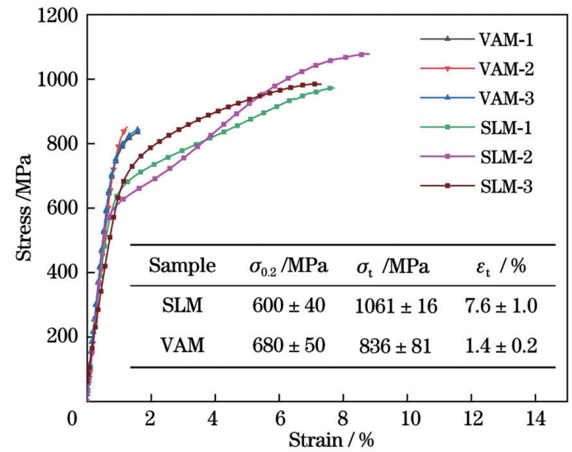

图 5　不同工艺条件下 Ti-1023 拉伸试样的应力-应变曲线

Fig. 5　Stress-strain curves of Ti-1023 tensile specimen under different process conditions

图 6 为不同工艺条件下 Ti-1023 拉伸试样的断口。可以看出，VAM 拉伸试样的断口中没有明显的宏观塑性变形区域，断裂面与拉伸方向垂直，整体呈现山脊状，存在大量的撕裂棱，同时光滑断裂面上存在河流花样，如图 6（c）所示。而 SLM 拉伸试样的断口存在大小不一的韧窝，大韧窝周围存在大量的小韧窝。说明 VAM 试样呈现典型脆性断裂特征，而 SLM 试样为韧性断裂。

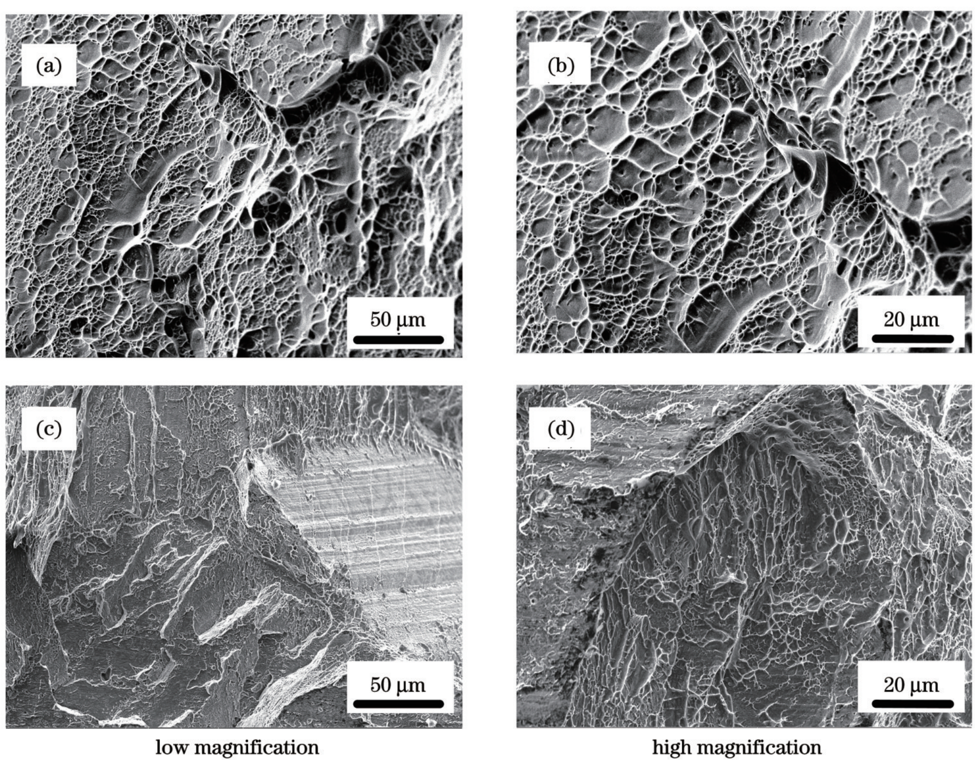

图 6　不同工艺条件下 Ti-1023 拉伸试样的断口。(a)(b) SLM Ti-1023；(c)(d) VAM Ti-1023

Fig. 6　Fractures of Ti-1023 tensile specimen under different process conditions. (a)(b) SLM Ti-1023; (c)(d) VAM Ti-1023

4　分析讨论

图 7 为不同工艺下 Ti-1023 合金的局部取向差（KAM），局部取向差可用来度量金属样品中的位错密度平均水平，即以取向差平均值作为位错密度的量化指标。位错密度对金属材料具有显著影响[30]。如图 7（a）、（b）所示，VAM 试样的平均 KAM 为 0.556°，几何位错密度（GND）为 1.29×10^{15} mm^{-2}，而 SLM 试样的平均 KAM 为 1.17°，几何位错密度为 2.72×10^{15} mm^{-2}。VAM 试样和 SLM 试样的几何位错更容易在晶界处聚集和塞积，晶界处的 KAM 及几何位错密度高于晶内。SLM 试样的晶粒尺寸较小，晶界面积较大，且晶粒形貌规则，形成了密度较高的位错“网格”，其几何位错密度约为 VAM 试样的 2.1 倍。表明 SLM 试样相较于 VAM 试样更容易产生位错，而位错对力学性能具有重要影响。其原因主要是在增材过程中，受约束介质

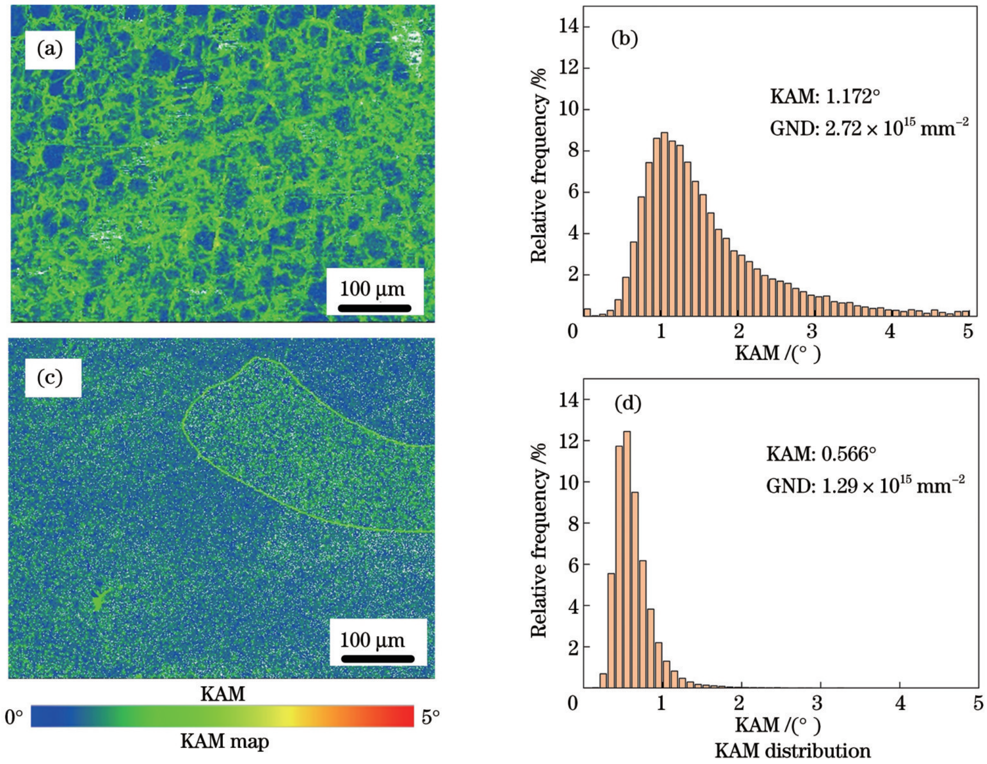

图 7　不同工艺下 Ti-1023 合金的 KAM。(a)(b) SLM Ti-1023 合金的 *XOY* 面；(c)(d) VAM Ti-1023 合金

Fig. 7　KAMs of Ti-1023 alloy under different process conditions. (a)(b) *XOY* face of SLM Ti-1023 alloy; (c)(d) VAM Ti-1023 alloy

的热膨胀/收缩引起的变形导致沉积层引入了高密度的位错[31-33]。同时 SLM 试样的平均晶粒尺寸为 47.32 μm，较小的晶粒尺寸意味着更多的晶界，在应力的作用下位错更容易在晶界处聚集和塞积。SLM 样品中的位错"网格"是不可动位错，其主要作用是协调晶格界面和保持材料连续性[34]。SLM 样品在制备过程中产生的位错"网格"在变形过程中阻碍位错运动，从而提高了 Ti-1023 材料的屈服强度。

亚稳 β 钛合金可利用 β 到 α 的相变实现强化效果，而力学性能如强度、塑性、韧性等都与其 α 相的含量、尺寸和形貌有极大关系。图 8 为 VAM 试样和 SLM 试样的微观形貌及相图。可以看出，VAM 试样针状的 α 相在 β 相晶界处大量聚集，在 β 晶粒内部呈弥散分布，α 相的体积分数为 3.11%。而 SLM 试样均为 β 相晶粒，

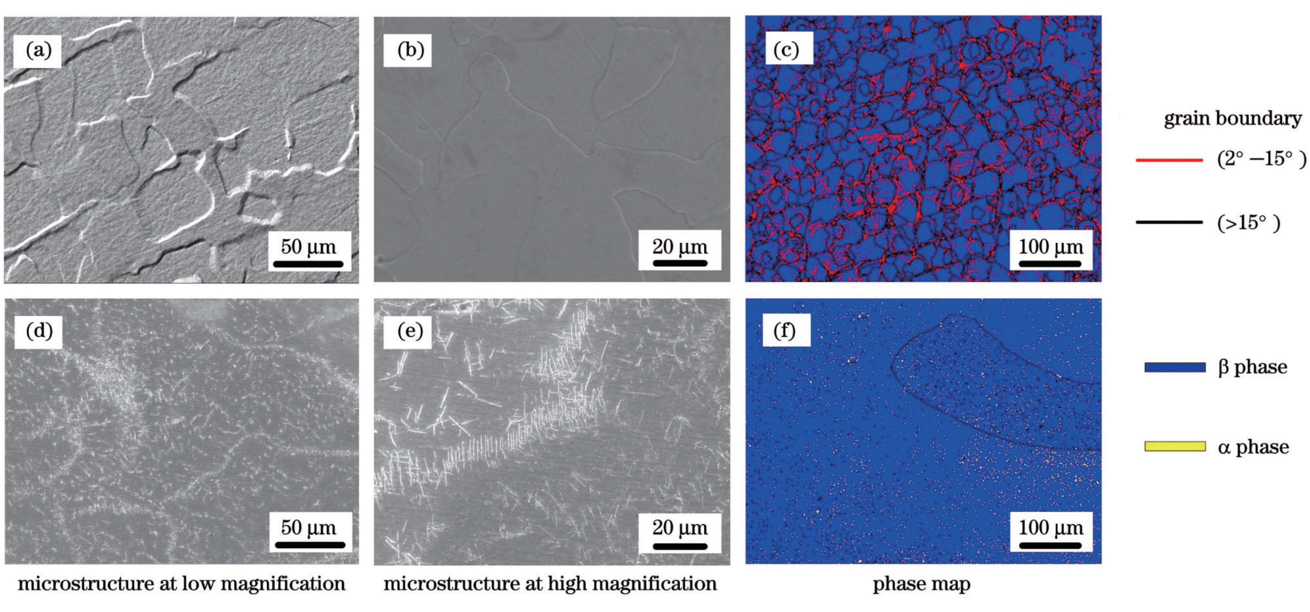

图 8　不同工艺下 Ti-1023 合金的显微组织及相图。(a)～(c) SLM Ti-1023 合金的 *XOY* 面；(d)～(f) VAM Ti-1023 合金

Fig. 8　Microstructures and phase diagrams of Ti-1023 alloy under different process conditions. (a)–(c) *XOY* face of SLM Ti-1023 alloy; (d)–(f) VAM Ti-1023 alloy β相晶粒内部无其他析出物。Deng 等[35]研究了 Ti-5Al-5Mo-5V-1Cr-1Fe(亚稳β钛合金 Ti-55511)中α相形貌、含量、尺寸对力学性能的影响,指出随着针状/板条状α相含量的增加,屈服强度和抗拉强度上升,塑性下降。因此,VAM 试样在冷却过程中产生了体积分数为 3.11% 的α相,屈服强度得到提高,但α相引入了相当数量的α/β界面,且α相不能形成具有相同取向的板条集束,这阻碍了变形过程中的位错滑移,导致延伸率下降为 1.4%。

图 9 为 SLM 试样和 VAM 试样在拉伸过程中的应变硬化率(应力对应变的一阶导数,即 $\frac{\partial \sigma_t}{\partial \varepsilon_t}$)、SLM 试样拉伸前后的 XRD 图及 SLM Ti-1023 断口截面的微观组织。如图 9(a)所示,VAM 试样进入屈服阶段后应变硬化率呈现直线下降,直至断裂。而 SLM 试样进入屈服阶段后,应变硬化率呈现下降(阶段Ⅰ)-上升(阶段Ⅱ)-下降(阶段Ⅲ)的变化趋势,其中最高上升量约为 1.9 GPa。对拉伸断裂后的 SLM 试样进行 XRD 检测,从 XRD 图可以看出,SLM 试样在断裂后产生了α相,形成了针状的马氏体α相,表明 SLM 试样在拉伸断裂过程中产生了相变,即部分β相转变为α相,这种现象被称为相变诱导塑性(TRIP)[36-37]。β相为体心立方(BCC)结构,相较于α相的密排六方(HCP)结构,具有较好的延展性,且亚稳β钛合金的β相具有机械不稳定性,外加应力可促使相变发生,进一步增加延伸率,在二者共同作用下,SLM 试样的延伸率相较于 VAM 试样得到了显著的提高。α相的含量会影响相变诱导塑性[38]。因此 VAM 试样进入屈服阶段后应变硬化率呈直线下降,VAM 试样的α相体积分数为 3.11%,阻碍了 VAM 试样相变诱导塑性强化机制的产生。

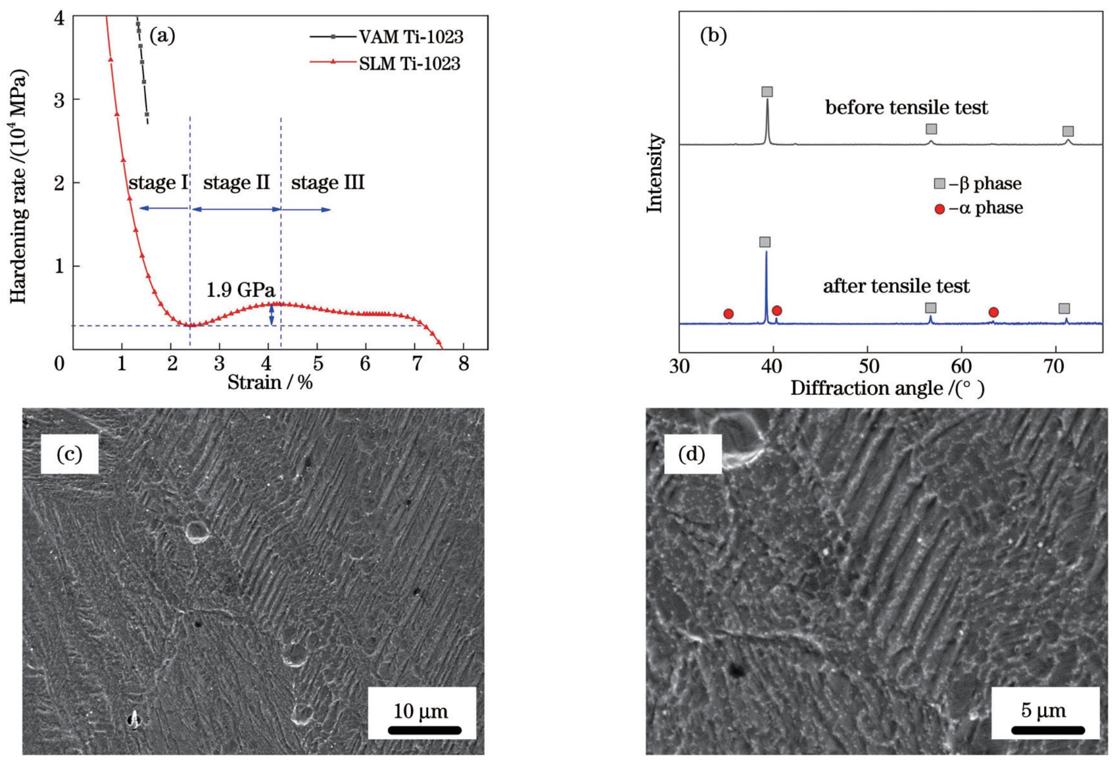

图 9 SLM 试样的拉伸数据。(a)应变硬化率;(b)SLM 试样拉伸测试前后 XRD 图;(c)SLM 断口 *XOY* 截面的低倍放大显微组织;(d)SLM 断口 *XOY* 截面的高倍放大显微组织

Fig. 9 Tensile data of SLM samples. (a) Strain hardening rate; (b) XRD patterns of SLM sample before and after tensile test; (c) microstructure of *XOY* cross section of SLM fracture at low magnification; (d) microstructure of *XOY* cross section of SLM fracture at high magnification

5 结 论

VAM Ti-1023 合金在冷却过程中发生了β到α的相变,产生了体积分数为 3.11% 的α相,室温组织由α+β两相构成;SLM Ti-1023 合金由于快速冷却,α相的产生得到抑制,室温组织由单一的β相构成。

SLM 样品缺少高硬度α相,但快速冷却条件带来的高密度位错阻碍了位错运动,使得其屈服强度与 VAM 试样相近。

SLM 试样的全β相组织避免了α/β界面的产生,并在变形中产生了应力诱导马氏体相变,使得断裂延伸率提升至 VAM 试样的 5 倍以上。

参 考 文 献

[1] Kolli R P, Devaraj A. A review of metastable beta titanium alloys[J]. Metals, 2018, 8(7): 506.

[2] Cotton J D, Briggs R D, Boyer R R, et al. State of the art in beta titanium alloys for airframe applications[J]. JOM, 2015, 67(6): 1281-1303.

[3] Balazic M, Kopac J, Jackson M J, et al. Review: titanium and titanium alloy applications in medicine[J]. International Journal of Nano and Biomaterials, 2007, 1(1): 3-34.
[4] 王向明，刘文珽 . 飞机钛合金结构设计与应用[M]. 北京：国防工业出版社，2010: 32.
Wang X M, Liu W T. Structural design and application of aircraft titanium alloy[M]. Beijing: National Defense Industry Press, 2010: 32.
[5] 杨家坤，包翔云，张金钰，等 . 亚稳β钛合金的设计方法及室温变形机制的研究进展[J]. 材料导报，2021, 35(19): 19170-19180.
Yang J K, Bao X Y, Zhang J Y, et al. A review on design methods and deformation mechanisms at room temperature of metastable β-titanium alloys[J]. Materials Reports, 2021, 35(19): 19170-19180.
[6] Kuroda D, Niinomi M, Morinaga M, et al. Design and mechanical properties of new β type titanium alloys for implant materials[J]. Materials Science and Engineering: A, 1998, 243(1/2): 244-249.
[7] Olakanmi E O. Selective laser sintering/melting (SLS/SLM) of pure Al, Al-Mg, and Al-Si Powders: effect of processing conditions and powder properties[J]. Journal of Materials Processing Technology, 2013, 213(8): 1387-1405.
[8] 张喜燕，赵永庆，白晨光 . 钛合金及应用[M]. 北京：化学工业出版社，2005: 73.
Zhang X Y, Zhao Y Q, Bai C G. Titanium alloy and its application [M]. Beijing: Chemical Industry Press, 2005: 73.
[9] 邵娟 . 钛合金及其应用研究进展[J]. 稀有金属与硬质合金，2007, 35(4): 61-65.
Shao J. Application and development of titanium alloys[J]. Rare Metals and Cemented Carbides, 2007, 35(4): 61-65.
[10] 刘全明，张朝晖，刘世锋，等 . 钛合金在航空航天及武器装备领域的应用与发展[J]. 钢铁研究学报，2015, 27(3): 1-4.
Liu Q M, Zhang Z H, Liu S F, et al. Application and development of titanium alloy in aerospace and military hardware [J]. Journal of Iron and Steel Research, 2015, 27(3): 1-4.
[11] 安国进 . 金属增材制造技术在航空航天领域的应用与展望[J]. 现代机械，2019(3): 39-43.
An G J. Application and prospect of metal additive manufacturing technology in aerospace[J]. Modern Machinery, 2019(3): 39-43.
[12] 巩水利，锁红波，李怀学 . 金属增材制造技术在航空领域的发展与应用[J]. 航空制造技术，2013, 56(13): 66-71.
Gong S L, Suo H B, Li H X. Development and application of metal additive manufacturing technology in aviation field[J]. Aeronautical Manufacturing Technology, 2013, 56(13): 66-71.
[13] Hu J Y, Liu P, Sun S Y, et al. Relation between heat treatment processes and microstructural characteristics of 7075 Al alloy fabricated by SLM[J]. Vacuum, 2020, 177: 109404.
[14] Gu D D, Meiners W, Wissenbach K, et al. Laser additive manufacturing of metallic components: materials, processes and mechanisms[J]. International Materials Reviews, 2012, 57(3): 133-164.
[15] Zheng B, Zhou Y, Smugeresky J E, et al. Thermal behavior and microstructural evolution during laser deposition with laser-engineered net shaping: part I. numerical calculations[J]. Metallurgical and Materials Transactions A, 2008, 39(9): 2228-2236.
[16] Joseph J, Jarvis T, Wu X H, et al. Comparative study of the microstructures and mechanical properties of direct laser fabricated and arc-melted Al_xCoCrFeNi high entropy alloys[J]. Materials Science and Engineering: A, 2015, 633: 184-193.
[17] Zhang W, Chabok A, Kooi B J, et al. Additive manufactured high entropy alloys: a review of the microstructure and properties[J]. Materials & Design, 2022, 220: 110875.
[18] Montero Sistiaga M, Nardone S, Hautfenne C, et al. Effect of heat treatment of 316L stainless steel produced by selective laser melting (SLM)[EB/OL]. [2023-02-03]. http://utw10945.utweb.utexas.edu/sites/default/files/2016/041-Sistiaga.pdf.
[19] 赵宇辉，贺晨，赵吉宾，等 . 增材/等材复合制备 Sc/Zr 改性 Al-Mg合金工艺研究[J]. 光学学报，2023, 43(7): 0716002.
Zhao Y H, He C, Zhao J B, et al. Process of Sc/Zr-modified Al-Mg alloy prepared by additive/equivalent composite manufacturing [J]. Acta Optica Sinica, 2023, 43(7): 0716002.
[20] 孙长进，赵吉宾，赵宇辉，等 . TA15钛合金激光熔化沉积工艺参数对超声检测精度的影响[J]. 光学学报，2019, 39(10): 1014002.
Sun C J, Zhao J B, Zhao Y H, et al. Effects of laser melting deposition process parameters on ultrasonic testing accuracy of TA15 titanium alloy[J]. Acta Optica Sinica, 2019, 39(10): 1014002.
[21] 赵宇辉，贺晨，邹健，等 . 外场对激光熔化沉积Al-Mg-Sc-Zr合金组织性能的影响[J]. 光学学报，2023, 43(2): 0214002.
Zhao Y H, He C, Zou J, et al. Effect of external field on microstructure and properties of Al-Mg-Sc-Zr alloy prepared by laser melting deposition[J]. Acta Optica Sinica, 2023, 43(2): 0214002.
[22] Yao D Z, Liu X H, Wang J, et al. Numerical insights on the spreading of practical 316 L stainless steel powder in SLM additive manufacturing[J]. Powder Technology, 2021, 390: 197-208.
[23] Agius D, Kourousis K I, Wallbrink C, et al. Cyclic plasticity and microstructure of as-built SLM Ti-6Al-4V: the effect of build orientation[J]. Materials Science and Engineering: A, 2017, 701: 85-100.
[24] Khorasani A M, Gibson I, Ghaderi A, et al. Investigation on the effect of heat treatment and process parameters on the tensile behaviour of SLM Ti-6Al-4V parts[J]. The International Journal of Advanced Manufacturing Technology, 2019, 101(9): 3183-3197.
[25] Cao S, Chu R K, Zhou X G, et al. Role of martensite decomposition in tensile properties of selective laser melted Ti-6Al-4V[J]. Journal of Alloys and Compounds, 2018, 744: 357-363.
[26] Jiang J J, Ren Z H, Ma Z B, et al. Mechanical properties and microstructural evolution of TA15 Ti alloy processed by selective laser melting before and after annealing[J]. Materials Science and Engineering: A, 2020, 772: 138742.
[27] Schwab H, Bönisch M, Giebeler L, et al. Processing of Ti-5553 with improved mechanical properties via an *in situ* heat treatment combining selective laser melting and substrate plate heating[J]. Materials & Design, 2017, 130: 83-89.
[28] Wang J C, Liu Y J, Qin P, et al. Selective laser melting of Ti-35Nb composite from elemental powder mixture: microstructure, mechanical behavior and corrosion behavior[J]. Materials Science and Engineering: A, 2019, 760: 214-224.
[29] 万明攀 . Ti-1300合金室温变形与组织演变研究[D]. 西安：西北工业大学，2015: 105.
Wan M P. Study on deformation and microstructure evolution of Ti-1300 alloy at room temperature[D]. Xi 'an: Northwestern Polytechnical University, 2015: 105.
[30] 杨平 . 电子背散射衍射技术及其应用[M]. 北京：冶金工业出版社，2007: 84-88.
Yang P. Electron backscattering diffraction technology and its application[M]. Beijing: Metallurgical Industry Press, 2007: 84-88.
[31] Liu L F, Ding Q Q, Zhong Y, et al. Dislocation network in additive manufactured steel breaks strength-ductility trade-off[J]. Materials Today, 2018, 21(4): 354-361.
[32] Gorsse S, Hutchinson C, Gouné M, et al. Additive manufacturing of metals: a brief review of the characteristic microstructures and properties of steels, Ti-6Al-4V and high-entropy alloys[J]. Science and Technology of Advanced Materials, 2017, 18(1): 584-610.
[33] Yamanaka K, Kuroda A, Ito M, et al. Quantifying the dislocation structures of additively manufactured Ti-6Al-4V alloys using X-ray diffraction line profile analysis[J]. Additive Manufacturing, 2021, 37: 101678.
[34] Lin D Y, Xu L Y, Jing H Y, et al. Effects of annealing on the structure and mechanical properties of FeCoCrNi high-entropy alloy fabricated via selective laser melting[J]. Additive Manufacturing, 2020, 32: 101058.
[35] Deng H, Qiu W B, Chen L Q, et al. Microstructure and

mechanical property of Ti-5Al-5Mo-5V-3Cr-1Zr alloy fabricated by selective laser melting with a preheated substrate[J]. Advanced Engineering Materials, 2021, 23(9): 2100265.

[36] Qi L C, Qiao X L, Huang L J, et al. Effect of cold rolling deformation on the microstructure and properties of Ti-10V-2Fe-3Al alloy[J]. Materials Characterization, 2019, 155: 109789.

[37] Ma X K, Li F G, Cao J, et al. Strain rate effects on tensile deformation behaviors of Ti-10V-2Fe-3Al alloy undergoing stress-induced martensitic transformation[J]. Materials Science and Engineering: A, 2018, 710: 1-9.

[38] Chen Z, Zhong D L, Sun Q, et al. Effect of α phase fraction on the dynamic mechanical behavior of a dual-phase metastable β titanium alloy Ti-10V-2Fe-3Al[J]. Materials Science and Engineering: A, 2021, 816: 141322.

Research on Microstructure and Mechanical Properties of Ti-1023 Alloy by Selective Laser Melting

Yang Ziwei[1,2], Xu Junqiang[1,2], Guo Shun[1,2], Wu Wendi[1,2], Zhou Qi[1,2*]

[1]*School of Materials Science and Engineering, Nanjing University of Science and Technology, Nanjing* 210094, *Jiangsu, China*;

[2]*Key Laboratory of Controlled Arc Intelligent Additive Manufacturing Technology, Ministry of Industry and Information Technology, Nanjing* 210094, *Jiangsu, China*

Abstract

Objective Metastable β titanium alloy has a high melting point, high activity, low thermal conductivity, and high deformation resistance. However, traditional manufacturing methods face several problems when dealing with the complex components of metastable β titanium alloys, such as numerous processes, long cycles, high cost, and low yield. Laser selective melting (SLM) is a new manufacturing technology that uses a laser as the heat source to melt metal powders layer-by-layer to manufacture solid parts. Owing to its super-complex structure forming ability, high material utilization rate, and rapid prototyping manufacturing ability, SLM provides an excellent solution for the manufacturing of titanium alloy parts with complex structures in aerospace. For the initial manufacturing process of metastable β titanium alloy, the cooling rate range of SLM is 10^3–10^8 K/s^{-1}, while that of traditional vacuum arc melting (VAM) is 10^1–10^2 K/s^{-1}. Non-equilibrium solidification resulting from rapid cooling is advantageous for grain refinement. The grain sizes of the SLM samples are significantly smaller than those of the VAM samples, and the grain size has a significant impact on their mechanical properties. The VAM Ti-1023 alloy is used to simulate the as-cast microstructure of a Ti-1023 alloy. The differences in the microstructures and mechanical properties of the SLM and VAM Ti-1023 alloys are compared. The effects of rapid cooling conditions on the microstructure and properties of Ti-1023 alloy are systematically studied and provide a theoretical basis for the additive manufacturing of complex components of metastable β titanium alloy.

Methods The SLM samples are fabricated using the Ti-1023 alloy powder prepared by gas atomization through laser selective melting. Figure 1 illustrates the morphology and particle size of the Ti-1023 powder. A laser metal powder 3D printer is used to produce the SLM samples. The laser spot diameter is 70 μm, and 20 mm×20 mm×10 mm blocks are directly deposited on a commercial Ti-6Al-4V substrate as shown in Fig. 2(a). Table 1 lists the elemental contents of both the Ti-6Al-4V substrate and Ti-1023 powder. In the preparation process, a laser power of 250 W, scanning speed of 1100 mm/s, scanning spacing of 60 μm, powder thickness of 30 μm, and rotation scanning strategy of 67° are employed as illustrated in Fig. 2(b). The sample with a relative density of 99.9% can be obtained by using Archimedes method.

The VAM samples are prepared on a commercial Ti-1023 alloy plate. The elemental composition of the commercial Ti-1023 alloy plate is listed in Table 1. The treated raw materials are placed in a water-cooled copper crucible in a VAM furnace. The furnace is first vacuumed to a gas pressure of 5×10^{-4} Pa, and then filled with argon . After three times, the ambient oxygen content is reduce to avoid sample oxidation. The surfaces of the VAM and SLM samples are then treated using a vibration-polishing equipment. The vibration-polishing frequency and polishing time are set to 56 Hz and 16 h, respectively. Next, the microstructures of the samples are observed and analyzed using an X-ray diffractometer, optical microscope, scanning electron microscope, and electron backscatter diffraction equipment. The tensile properties of the Ti-1023 samples under different processes are tested using a universal mechanical testing machine. The tensile tests are performed at room temperature at a tensile speed of 0.1 mm/min.

Results and Discussions As shown in Fig. 3, the phase composition of the VAM sample is α+β phases, and the SLM sample is mainly composed of β phase. It is shown that the SLM rapid cooling condition inhibits the phase transition process of β→α and a full β-phase structure forms, while the VAM sample is composed of an α+β dual phase structure. Under rapid SLM cooling, the grain size is approximately 1/10 that of VAM as shown in Fig. 4. The acicular α phase with volume fraction of 3.11% forms in the VAM sample during cooling. Simultaneously, the acicular α phase accumulates at the grain boundary of the β phase and disperses inside the β grains as shown in Fig. 8. Although the SLM sample lacks a high-hardness α phase, the high-density dislocation caused by the rapid cooling conditions is 2.1 times that of the VAM sample as shown in Fig. 7. The dislocation grid is an immovable dislocation, and its main role is to coordinate the lattice interface and maintain material continuity. Dislocation movement is hindered during the deformation process, thereby improving the yield strength of Ti-1023. The full β-phase structure of the SLM sample avoids the formation of the α/β interface and produces stress-induced martensitic transformation during deformation as shown in Fig. 9. The stress-induced martensitic transformation can increase the fracture elongation by more than five times that of the VAM sample as shown in Fig. 5.

Conclusions During the cooling process of VAM Ti-1023 alloy, the phase transition from β to α occurs, and the acicular α phase with volume fraction of 3.11% is produced. The microstructure at room temperature is composed of α+β phases. Because of the rapid cooling of the SLM Ti-1023 alloy, the formation of the β phase is inhibited, and the room-temperature structure is composed of single β phase.

SLM samples lack a high hardness α phase and their yield strength is comparable to that of VAM samples owing to the presence of high-density dislocations, which inhibit dislocation movement under rapid cooling conditions.

The full β-phase structure of the SLM sample avoids the formation of the α/β interface. As a result, stress-induced martensitic transformation occurs during deformation, leading to an increase in fracture elongation by more than five times that of the VAM samples.

Key words laser technique; Ti-1023; selective laser melting; vacuum arc melting; microstructure; mechanical properties